Songklanakarin J. Sci. Technol.
47 (1), 65–71, Jan. – Feb. 2025

http://www.sjst.psu.ac.th

*Original Article*

# Deformation behavior and flow stress determination of AISI 8620 steel

Visarut Phatiwach[1], Oranicha Theerakiat[1], Laksamee Angkurarach[2], and Patiphan Juijerm[1*]

[1] *Department of Materials Engineering, Faculty of Engineering, Kasetsart University, Chatuchak, Bangkok, 10900 Thailand*

[2] *Division of Material and Process Engineering Technology, Faculty of Engineering and Technology, King Mongkut's University of Technology North Bangkok, Rayong Campus, Nonglalok, Ban Khai, Rayong, 21120 Thailand*

Received: 2 June 2023; Revised: 6 August 2024; Accepted: 29 November 2024

## Abstract

Mechanical properties and deformation behavior of AISI 8620 steel were investigated and intensively analyzed. Kocks-Mecking (K-M) and Crussard-Jaoul (C-J) analyses were applied to describe the deformation behavior. Flow stresses, yield point, and instability were predicted and compared with experimental data using various constitutive models, namely Ludwik, Hollomon, Swift, Ludwigson, Voce, and artificial neuron network (ANN). It was found that the plastic deformation behavior of the AISI 8620 steel was in stage III with a single negative slope value. Two different plastic deformation zones were observed. All constitutive and ANN models excellently predicted the flow stresses in the range of uniform plastic deformation between the yield point and the instability. The yield point and instability with errors less than 4 and 6% could be predicted, respectively, using Ludwik, Hollomon, Swift, Ludwigson, and Voce models, whereas the ANN model accurately determined the yield stress and instability.

**Keywords**: strain hardening, mechanical property, flow curve, plastic deformation, neuron network

## 1. Introduction

AISI 8620 steel is widely selected in the automotive and aerospace industries because of its high intensity, high toughness, good hardenability, and stability in resisting overheating (Çelik, Efeoglu, & Sakar, 2001; Lu *et al*., 2011). Moreover, the alloying elements, such as Cr, Ni, and Mo in AISI 8620 steel, provide a high potential for various surface treatments to improve its wear and corrosion resistances for more complex applications (Çelik *et al*., 2001; Gunes, Ulker, & Taktak, 2011; Tabur, Izciler, Gul, & Karacan, 2009). Therefore, the AISI 8620 steel is related to engineering, especially mechanical properties, design, and manufacturing. Nowadays, engineering designs and manufacturing processes are becoming more sophisticated and advanced because precise forming and manufacturing processes are more in demand. Thus, computer-aided engineering (CAE) and manufacturing (CAM) are essential in precision manufacturing. The calculations and simulations of computer-aided engineering and manufacturing are well established in terms of accurate mechanical properties and an excellent understanding of the deformation behavior of metallic materials, especially in the plastic deformation region. In commercial CAE/CAM software, empirical parameters from experimental or test data are necessary for calculation and simulation. Tensile testing is one of the most well-known mechanical testing methods. A uniaxial stress-strain relationship in elastic, elastic-plastic, and plastic regions of investigated metallic materials is provided (Ghosh & Ghosh, 2018). The deformation behavior in the plastic region after the proportional limit to ultimate tensile strength (UTS) is necessary information used in metal forming design, particularly when more precise forming is expected. Therefore, understanding plastic deformation behavior is crucial and shall be addressed. There are several constitutive equations, i.e., Ludwik (Ludwik, 1909), Hollomon (Hollomon, 1945), Swift (Swift, 1952), Ludwigson (Ludwigson, 1971), and

*Corresponding author
Email address: fengppj@ku.ac.th; juijerm@gmail.com

Voce (Voce, 1948) describing the relationship between stress and strain in the plastic region.

Moreover, machine learning using an artificial neural network (ANN), was a recent alternative approach to modeling materials and processing techniques (J. Ghaboussi, J. H. Garrett Jr., 1991; Lee, Shin, & Hwang, 2021; Lin, Zhang, & Zhong, 2008; Lourenço, Andrade-Campos, & Georgieva, 2022). ANN principally learns from examples or experimental data by recognizing patterns in a series of input and output values. Thus, prior assumptions are required, and physical knowledge about deformation is not incorporated (Haghdadi, Zarei-Hanzaki, Khalesian, & Abedi, 2013). From this point of view, prediction and analysis of the deformation behavior and flow curves using ANN are of particular interest. Furthermore, the essential mechanical properties from tensile testing, i.e., yield stress and instability, can be analyzed and determined using these constitutive equations and ANN. The intensive analysis, empirical parameters, and determination of tensile properties in this research will provide useful guidance for other metals in practice.

Therefore, in this research, the plastic deformation under tensile loading of the AISI 8620 steel was intensively analyzed using Ludwik, Hollomon, Swift, Ludwigson, Voce, and ANN models. Flow stresses were predicted using these constitutive and ANN models. The parameters and material constants determined from experimental data are reported. The sum of squares of deviations of the prediction (Chi-square, $\chi^2$), the coefficient of determination ($R^2$), and the mean absolute percentage error (MAPE) were calculated to validate the parameters and materials constants of the constitutive models. Strain hardening behavior was analyzed using the Kocks-Mecking (K-M) (Kocks, 1976; Kocks & Mecking, 2003; Mecking & Kocks, 1981; Mondal, Singh, Mukhopadhyay, & Chattopadhyay, 2013) and Crussard-Jaoul (C-J) (Crussard & Jaoul, 1950) analysis. Finally, the yield stress and instability of the AISI 8620 steel were estimated using the constitutive and ANN models and then compared with experimental values.

## 2. Materials and Methods

The AISI 8620 steel was delivered as hot-rolled bars with a diameter of 40 mm. The chemical composition of this alloy is 0.21 C, 0.85 Mn, 0.02 P, 0.04 S, 0.29 Si, 0.44 Ni, 0.57 Cr, 0.16 Mo, and Fe for the remainder in balance (all values in wt.%). Specimens of 6×6 mm cross section and a gauge length of 25 mm were prepared following ASTM E8 for tensile tests. The tensile loading direction corresponds to the rolling direction of the bar. Tensile tests were performed at a constant strain rate of $10^{-3}$ $s^{-1}$ using the universal testing machine Instron model 5985. The true stress-strain curve was analyzed. The true plastic strain was determined by subtracting the elastic strain from the true total strain. The plastic deformation was analyzed using Ludwik, Hollomon, Swift, Ludwigson, and Voce models, shown in Equations (1)-(5). The $\sigma$ is true stress, $\varepsilon$ is true strain, $k$ is the strength coefficient, $n$ is the strain hardening exponent, and $A$ and $\beta$ are material constants.

The strain hardening rates derived from Ludwik, Swift, and Voce are shown in Equations (6)-(8). K-M analysis, differential C-J, and modified C-J (CAO, LI, MA, & SUN, 2017; Das & Chattopadhyay, 2009; Son, Lee, Park, Lee, & Shin, 2005) are considered based on the strain hardening rate, as shown in Equations (9)-(11).

Constitutive models:

Ludwik: $$\sigma = \sigma_0^L + k_L\varepsilon^{n_L} \quad (1)$$

Hollomon: $$\sigma = k_H\varepsilon^{n_H} \quad (2)$$

Swift: $$\sigma = k_S(\varepsilon_0 + \varepsilon)^{n_S} \quad (3)$$

Ludwigson: $$\sigma = k_1\varepsilon^{n_1} + e^{k_2}.e^{n_2\varepsilon} \quad (4)$$

Voce: $$\sigma = \sigma_0\left(1 - Ae^{-\beta\varepsilon}\right) \quad (5)$$

Strain hardening rate:

Strain hardening rate of Ludwik:
$$d\sigma/d\varepsilon = d\sigma_0/d\varepsilon + kn\varepsilon^{n-1} \quad (6)$$

Strain hardening rate of Swift:
$$d\sigma/d\varepsilon = nk^{1/n}\sigma^{1-1/n} \quad (7)$$

Strain hardening rate of Voce:
$$d\sigma/d\varepsilon = A\beta\sigma_s e^{(-\beta\varepsilon)} = \beta(\sigma_s - \sigma) \quad (8)$$

Analytical models (from Equation (6)-(8)):

Differential C-J:
$$\ln(d\sigma/d\varepsilon) = \ln\left(k_{CJ}n_{CJ}\right) + \left(n_{CJ} - 1\right)\ln\varepsilon \quad (9)$$

Modified C-J:
$$(d\sigma/d\varepsilon) = \ln\left(nk^{1/n}\right) + (1 - 1/n)\ln\sigma \quad (10)$$

K-M analysis:
$$d\sigma/d\varepsilon = \theta_0 - \beta\sigma;\theta_0 = \beta\sigma_s \quad (11)$$

The ANN model has three layers of neurons: input layer, hidden layer, and output layer, as shown in Figure 1. The weights and bias values connect the neurons in the network. The information from the input layer is processed through the hidden layer. The input signal was broadcast to all neurons in the hidden layer. Each neuron appended its weighted input signal, including bias value, and then the activation function was applied to compute the output signal of each neuron in the hidden layer, as illustrated in Equation (12). The output layer was connected to the hidden layer through the weights ($W_{jk}$) and biases ($b_k$), as shown in Equation (13). The ANN was performed without any material behavior concern, making it superior to the above constitutive models (Chun, Biglou, Lenard, & Kim, 1998; Genel, 2004; Sabokpa, Zarei-Hanzaki, Abedi, & Haghdadi, 2012).

$$h_j = f\left(\sum_{i=1}^{n} W_{ij}X_i + b_j\right) \quad (12)$$

$$Y_k = f\left(\sum_{j=1}^{m} W_{jk}h_j + b_k\right) \quad (13)$$

Activation function:
$$f(x) = \frac{2}{1 + e^{-2x}} - 1 \quad (14)$$

Mean square error:
$$MSE = \frac{1}{N}\sum_{i=1}^{N}\left(Y_i' - Y_i\right)^2 \quad (15)$$

Root mean square error:
$$RMSE = \sqrt{\frac{1}{N}\sum_{i=1}^{N}\left(Y_i' - Y_i\right)^2} \quad (16)$$

where $X$ is the input vector, $Y$ is the output vector, $h$ is the vector of neurons in the hidden layer, $W$ is weights, $b$ is biases, and $i$, $j$, and $k$ are the labels of neurons in the input, hidden, and

output layers, respectively. The activation function (*f*) in this research is a hyperbolic tangent sigmoid (tansig), as shown in Equation (14). The back-propagation training algorithm is an iterative gradient algorithm, designed to minimize the mean square error (MSE) between the predicted output (*Y'*) and the desired output (*Y*). The weights and biases were updated according to Levenberg-Marquardt optimization. The ANN in this work was designed and trained using MATLAB. The dataset was randomly divided into three groups: 75% for the training set, 15% for the validation set, and 15% for the test set. The input layer consisted of one feature, which was the true strain. One hidden layer with thirteen neurons was used. The output was the true stress.

Finally, the predictive performance, the coefficient of determination ($R^2$), Chi-square ($\chi^2$), and the mean absolute percentage error (*MAPE*) were quantitatively obtained based on regression analysis. The *MAPE* is defined as follows.

$$MAPE = \frac{1}{n}\sum_{i=1}^{n}\left|\frac{E_i - P_i}{E_i}\right| \times 100 \quad (17)$$

where *E* are the data from experiments, and *P* are the data from the prediction.

## 3. Results and Discussion

### 3.1 Microstructure, stress-strain curve, and tensile properties

The microstructure of the AISI 8620 steel is composed of ferrite and pearlite structures in equiaxed grains with an average grain size of 21.67 μm. The fractions of ferrite and pearlite were about 74.5% and 25.5%, respectively. The Brinell hardness, tested five times, gave an average hardness of 194 HBW. The true stress-strain (flow) curve is plotted in Figure 2. The yield stress of 430.95 MPa was determined using the intersection of the 0.2% offset line and stress-strain curve (Figure 2). The UTS of the engineering stress-strain curve was about 573.726 MPa, which corresponds to the instability of the true stress-strain curve. The true stress at the instability of about 620.545 MPa was calculated.

### 3.2 Deformation behavior

The deformation behavior of metallic materials can be explored and analyzed via strain hardening rate during the plastic deformation. Thus, the strain hardening rate was first plotted versus the true stress followed by the K-M analysis in Equation (11), as shown in Figure 4. The deformation behavior of a metallic material was explained by the strain hardening rate in five stages. Stage I corresponded to a low level of strain hardening in single crystals oriented for a glide on a single slip system. For a polycrystalline metallic material, the deformation in stage I is not considered. Stage II is described as athermal hardening. Plastic strains occurred by dislocation movements, and then the dislocation interactions and multiplications led to increased resistance to plastic flow. However, the opposite-sign dislocation can be annihilated, leading to a dynamic recovery, a softening process occurring concurrently with plastic strain. Stage III corresponds to the regime where the strain hardening rate decreases linearly as the flow stress increases. At larger strains, a breakdown of the linear decrease of the strain

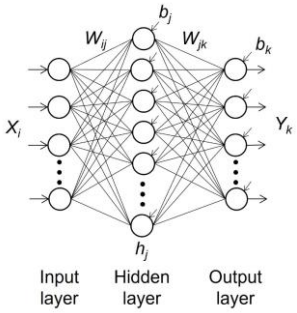


Figure 1. The structure of a three-layer ANN

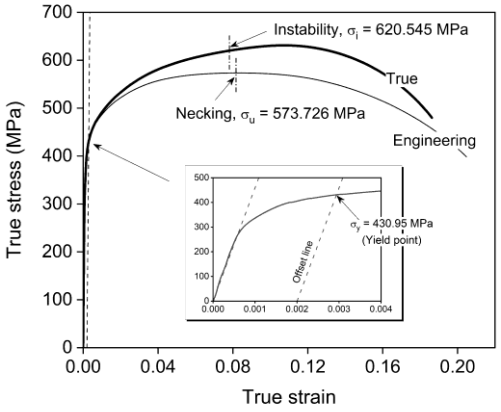


Figure 2. Engineering and true stress-strain curves of AISI 8620 steel

hardening rate is referred to as stage IV. The dislocation debris accumulates and then increases the strain hardening. In the final stage V, before the stress saturates, the strain hardening rate is constant at a very low value. Finally, the strain hardening ends (Embury, & Lloyd, 2011; Embury, Poole, & Lloyd, 2006; Pandre, Mhatre, Kotkunde, & Kumar Singh, 2019; Poole, Rollett & Kocks, 1993). The plastic deformation behavior of the AISI 8620 steel in Figure 4 exhibited dynamic recovery in a linear relation in stage III. The dislocation annihilation parameter $\beta$ of 0.036 was determined by the slope in stage III. The dislocation storage $\theta_0$ of 22.435 was determined by the y-axis intersection at the true stress zero. The stage IV was not observed in the AISI 8620 steel. The instability criterion referred to as the UTS in the engineering stress-strain curve could be revealed by the point that has the strain hardening rate equal to the true stress ($d\sigma/d\varepsilon = \sigma_T$) (Dieter, 1988; Tomita & Okabayashi, 1985; Voce, 1948). The instability at the true stress of about 620.545 MPa was determined.

The Modified C-J in Equation (10) allows analysis based on the Swift model. The double logarithmic diagram of the strain hardening rate as a function of the true stress was constructed and assessed. Many researchers have reported that the ferrite-pearlite, especially with a low pearlite fraction, shows only a single slope in the modified C-J compared with the ferrite-martensite structure in dual-phase steels. However, when the modified C-J analysis of the ferrite-pearlite structure was precisely considered, it was found that the deformation of the ferrite-pearlite structure exhibited a behavior of a dual-phase steel. The modified C-J analysis of the AISI 8620 steel is

shown in Figure 4. The elastic-plastic transition zone was referred to as a transient stage and the glide of mobile dislocations in the ferrite phase. Next to the elastic-plastic transition zone was stage III of the K-M analysis (Figure 3), where zones I and II with slopes of -6.387 and -14.186 were detected, respectively. The zone I corresponded to the deformation of constrained ferrite. Finally, zone II was related to the concurrent deformation of hardened ferrite (or martensite in dual-phase steel) (Alibeyki, Mirzadeh, Najafi, & Kalhor, 2017; Das & Chattopadhyay, 2009; Ghatei Kalashami, Kermanpur, Ghassemali, Najafizadeh, & Mazaheri, 2016; Mirzadeh, Alibeyki, & Najafi, 2017; Nasiri & Mirzadeh, 2018; Tomita & Okabayashi, 1985).

The differential C-J analysis of the AISI 8620 steel was constructed using a double logarithmic diagram of the strain hardening rate versus the true strain, as shown in Figure 5. Two zones are identical to the modified C-J analysis. The deformation behavior analyzed using the differential C-J diagram in Figure 5 could be interpreted in the same ways as in the modified C-J diagram. The slopes of -0.713 and -1.375 were measured for zones I and II, respectively.

### 3.3 Flow stress prediction

The true stress-strain curve of AISI 8620 steel in a region between the yield point and the instability was analyzed using constitutive equations in Equation (1)-(5). All parameters and empirical constants were determined using non-linear curve fitting with the least squares method, as shown in Table 1. Moreover, $\chi^2$, $R^2$, and the *MAPE* were calculated to validate the estimated values of parameters and empirical constants. Flow stresses in a region between the proportional limit, and the instability were calculated using constitutive equations in Equation (1)-(5) with parameters and empirical constants in Table 1 and then plotted in Figure 6. After the instability, flow stresses were further calculated as extrapolation. The flow stresses from the experiment and calculation were plotted in one diagram to exhibit a deviation, as shown in Figure 8. It was found that all models, i.e., Ludwik, Hollomon, Swift, Ludwigson, and Voce, were excellent constitutive models to fit experimental data of the AISI 8620 steel if the plastic deformation was uniform between the yield point and the stability. The Voce model exhibited a higher deviation at low plastic strain than others. The extrapolated flow stresses after the instability possessed a very high deviation because all considered constitutive equations in Equation (1)-(5) were hardening type models that do not cover flow stress reduction after the instability or the necking phenomenon.

The flow stresses of the AISI 8620 steel were predicted using ANN. One hidden layer was found to be adequate for this problem. The number of neurons in the hidden layer was optimized by consideration of root mean square error (*RMSE*), as shown in Figure 7. Thus, the simulated flow stresses in Figure 6 were calculated from ANN with thirteen neurons in the hidden layer. $\chi^2$, $R^2$, and *MAPE* were also calculated to validate the ANN and are shown in Table 1. The results in Figure 6 show that the predicted stresses using ANN were very close to the experimental values. The $\chi^2$ and *MAPE* of the ANN were lowest, and $R^2$ was very close to 1. That indicated that the ANN model was superior to other constitutive models. Moreover, the ANN could accurately predict flow stresses for all strains, even after instability.

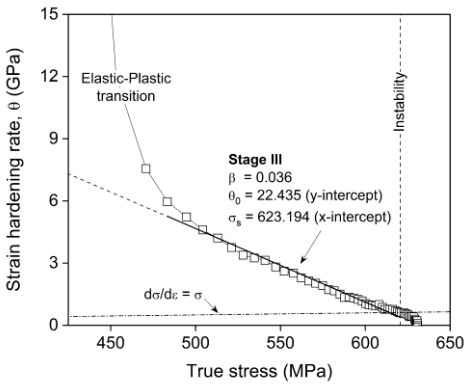


Figure 3. K-M analysis of AISI 8620 steel

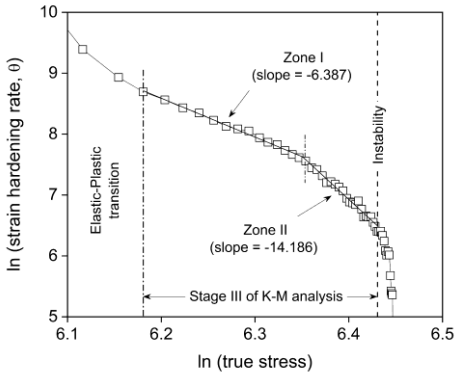


Figure 4. Modified C-J analysis of AISI 8620 steel

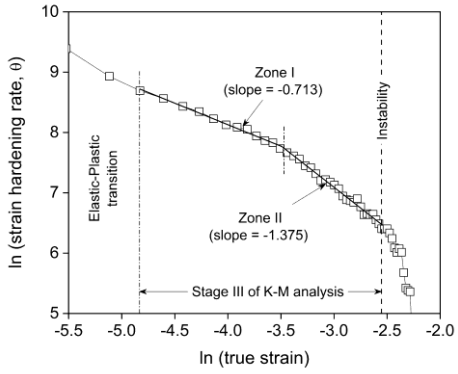


Figure 5. Differential C-J analysis of AISI 8620 steel

### 3.4 Yield stress and instability determination

The yield stress is usually determined using an intersection of the offset line with the flow curve, as shown in Figure 2. The yield stress of about 430.95 MPa was revealed. An estimate of the yield stress could be generated by considering the intersection of the offset line with the flow curve simulated using different models (Figure 6). Therefore,

Table 1. Parameters, empirical constants, $\chi^2$, $R^2$, and *MAPE* of various constitutive and ANN models

| Model | Parameters | Estimated value |
|---|---|---|
| Ludwik | $\sigma_0{}^L$ | 132.562 |
| | $k_L$ | 714.110 |
| | $n_L$ | 0.146 |
| | $\chi^2$ | 4.157 |
| | $R^2$ | 0.999 |
| | *MAPE* | 0.331% |
| Hollomon | $k_H$ | 824.162 |
| | $n_H$ | 0.110 |
| | $\chi^2$ | 5.054 |
| | $R^2$ | 0.998 |
| | *MAPE* | 0.367% |
| Swift | $\varepsilon_0$ | $6.512 \times 10^{-4}$ |
| | $k_s$ | 836.224 |
| | $n_s$ | 0.115 |
| | $\chi^2$ | 3.441 |
| | $R^2$ | 0.999 |
| | *MAPE* | 0.589% |
| Ludwigson | $k_1$ | 938.830 |
| | $n_1$ | 0.345 |
| | $k_2$ | 5.758 |
| | $n_2$ | -3.886 |
| | $\chi^2$ | 1.733 |
| | $R^2$ | 0.999 |
| | *MAPE* | 0.216% |
| Voce | $\sigma_0$ | 625.018 |
| | $A$ | 0.322 |
| | $\beta$ | 39.768 |
| | $\chi^2$ | 10.549 |
| | $R^2$ | 0.996 |
| | *MAPE* | 0.458% |
| ANN | $\chi^2$ | 0.183 |
| | $R^2$ | 0.999 |
| | *MAPE* | 0.046% |

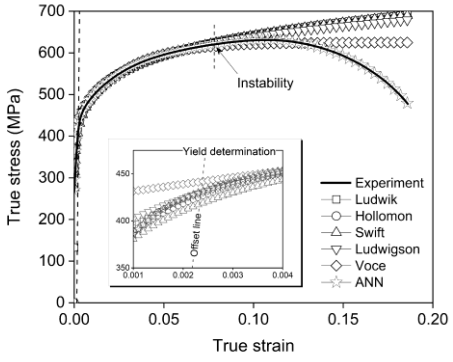


Figure 6. Simulated flow curves of AISI 8620 steel using various constitutive models

the yield stresses estimated using the Ludwik, Hollomon, Swift, Ludwigson, and Voce models are summarized with percentage errors in Table 2. All these models exhibited great precision of estimates of the yield stress.

From the experiment, the instability of 620.545 MPa in the true stress-strain curve was determined (Figure 2). For the prediction aspect, the instability criterion could be revealed

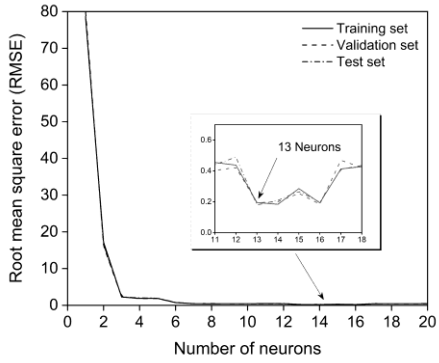


Figure 7. Root mean square error related to the number of neurons in the hidden layer

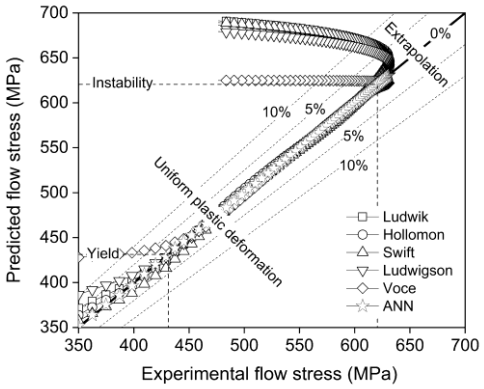


Figure 8. Comparison of predicted and experimental flow stresses of AISI 8620 steel

by the point at which the strain hardening rate is equal to the true stress ($d\sigma/d\varepsilon = \sigma_T$) (Dieter, 1988; Tomita & Okabayashi, 1985; Voce, 1948). Therefore, the strain hardening rates were calculated from the flow curves simulated by Ludwik, Hollomon, Swift, Ludwigson, and Voce in Figure 6 and then plotted in one diagram, as shown in Figure 9. The intersection of the calculated strain hardening rate and simulated flow curve in Figure 9 was the estimated instability. All estimated instability values with percentage errors are shown in Table 2. All models possessed an error lower than 6% compared with the experiment. Ludwigson and Voce exhibited a lower deviation than the other constitutive models. Nevertheless, the ANN provided superior predicted stresses for a wide range of strains, resulting in high accuracy and excellent yield stress and instability determination compared to the constitutive models.

## 4. Conclusions

The deformation behavior of the AISI 8620 steel was intensively analyzed. Flow curves, yield, and UTS were predicted using various constitutive and ANN models. Conclusions can be summarized as follows:

1. The K-M analysis revealed that the plastic deformation behavior of the AISI 8620 steel was in stage III with a single negative slope value (dynamic recovery) until it reached instability.

Table 2. Determined yield stress and instability using various constitutive and ANN models

| Model | Yield stress (MPa) | % Error of yield stress | Instability (MPa) | % Error of instability |
|---|---|---|---|---|
| Experiment | 430.950 | - | 620.545 | - |
| Ludwik | 427.682 | -0.758 | 654.238 | +5.430 |
| Hollomon | 425.961 | -1.158 | 647.177 | +4.292 |
| Swift | 417.741 | -3.065 | 652.073 | +5.081 |
| Ludwigson | 430.221 | -0.169 | 638.057 | +2.822 |
| Voce | 441.947 | +2.552 | 609.627 | -1.759 |
| ANN | 430.642 | +0.071 | 620.714 | +0.027 |

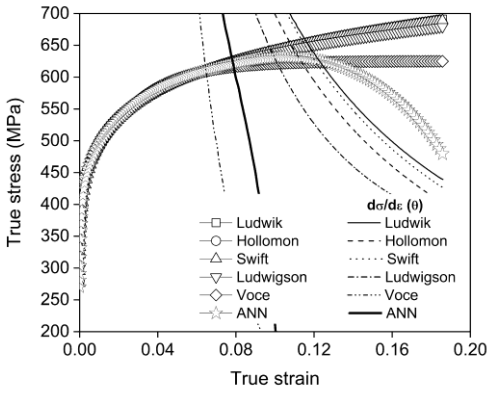


Figure 9. Instability determination of AISI 8620 steel

2. The modified and differential C-J analyses exhibited identical results, illustrating two deformation zones: zone I corresponded to the deformation of constrained ferrite, and zone II corresponded to the concurrent deformation of hardened ferrite.
3. Constitutive models, namely Ludwik, Hollomon, Swift, Ludwigson, and Voce, excellently predicted the flow stresses in the range of uniform plastic deformation. ANN model could accurately predict flow stresses for all strains, even after instability.
4. Using Ludwik, Hollomon, Swift, Ludwigson, and Voce models could determine yield stress and instability with an acceptable error. The ANN model accurately determined the yield stress and instability.

## Acknowledgements

The authors would like to gratefully thank the Graduate School, and Faculty of Engineering, Kasetsart University, Thailand, for financial support for Mr. Visarut Phatiwach and Oranicha Theerakiat. Thanks are also due to Mr. Kittiphong Nimarkorn for supporting some investigations.

## References

Alibeyki, M., Mirzadeh, H., Najafi, M., & Kalhor, A. (2017). Modification of rule of mixtures for estimation of the mechanical properties of dual-phase steels. *Journal of Materials Engineering and Performance*, *26*(6), 2683–2688. Retrieved from https://doi.org/10.1007/s11665-017-2687-6

CAO, J., LI, F. Guo, MA, X. Kai, & SUN, Z. Kun. (2017). Tensile stress–strain behavior of metallic alloys. *Transactions of Nonferrous Metals Society of China (English Edition)*, *27*(11), 2443–2453. Retrieved from https://doi.org/10.1016/S1003-6326(17)60271-1

Çelik, A., Efeoglu, I., & Sakar, G. (2001). Microstructure and structural behavior of ion-nitrided AISI 8620 steel. *Materials Characterization*, *46*(1), 39–44. Retrieved from https://doi.org/10.1016/S1044-5803(00)00091-7

Chun, M. S., Biglou, J., Lenard, J. G., & Kim, J. G. (1998). Using neural networks to predict parameters in the hot working of aluminum alloys. *Journal of Materials Processing Technology*, *86*(1–3), 245–251. Retrieved from https://doi.org/10.1016/S0924-0136(98)00318-5

Crussard, Ch., & Jaoul, B. (1950). Contribution à l'étude de la forme des courbes de traction des métaux et à son interprétation physique. *Revue de Métallurgie*, *47*(8), 589–600. Retrieved from https://doi.org/10.1051/metal/195047080589

Das, D., & Chattopadhyay, P. P. (2009). Influence of martensite morphology on the work-hardening behavior of high strength ferrite-martensite dual-phase steel. *Journal of Materials Science*, *44*(11), 2957–2965. Retrieved from https://doi.org/10.1007/ s10853-009-3392-0

Dieter, G. E. (1988). *Mechanical metallurgy, 1988, SI metric edition*. London, English: Grawhill Book Company.

Embury, J. D., Poole, W. J., & Lloyd, D. J. (2006). The work hardening of single phase and multi-phase aluminium alloys. *Materials Science Forum*, *519*, 71–78.

Genel, K. (2004). Application of artificial neural network for predicting strain-life fatigue properties of steels on the basis of tensile tests. *International Journal of Fatigue*, *26*(10), 1027–1035. Retrieved from https://doi.org/10.1016/j.ijfatigue.2004.03.009

Ghaboussi, J., Garrett, J. H., & Wu, X. (1991). Knowledge-based modeling of material behavior with neural networks. *Journal of Engineering Mechanics*, *117*(1), 132–153.

Ghatei Kalashami, A., Kermanpur, A., Ghassemali, E., Najafizadeh, A., & Mazaheri, Y. (2016). Correlation of microstructure and strain hardening behavior in the ultrafine-grained Nb-bearing dual phase steels. *Materials Science and Engineering A*, *678*, 215–226. Retrieved from https://doi.org/10.1016/j.msea.2016.09.108

Ghosh, A., & Ghosh, M. (2018). Tensile and impact behaviour of thermo mechanically treated and micro-alloyed medium carbon steel bar. *Construction and Building Materials*, *192*, 657–670. Retrieved from https://doi.org/10.1016/J.CON BUILDMAT.2018.10.098

Gunes, I., Ulker, S., & Taktak, S. (2011). Plasma paste boronizing of AISI 8620, 52100 and 440C steels. *Materials and Design*, *32*(4), 2380–2386. Retrieved from https://doi.org/10.1016/j.matdes.2010.11.031

Haghdadi, N., Zarei-Hanzaki, A., Khalesian, A. R., & Abedi, H. R. (2013). Artificial neural network modeling to predict the hot deformation behavior of an A356 aluminum alloy. *Materials and Design*, *49*, 386–391. Retrieved from https://doi.org/10.1016/j.matdes.2012.12.082

Hollomon, H. (1945). Tensile deformation. *Transactions of the Metallurgical Society of AIME*, *162*, 268-290.

Kocks, U. F. (1976). Laws for work-hardening and low-temperature creep. *Journal of Engineering Materials and Technology*, *98*(1), 76–85. Retrieved from https://doi.org/10.1115/1.3443340

Kocks, U. F., & Mecking, H. (2003, January 1). Physics and phenomenology of strain hardening: The FCC case. *Progress in Materials Science*, *48*, 171–273. Retrieved from https://doi.org/10.1016/S0079-6425(02)00003-8

Lee, S. I., Shin, S. H., & Hwang, B. C. (2021). Application of artificial neural network to the prediction of tensile properties in high-strength low-carbon bainitic steels. *Metals*, *11*(8). Retrieved from https://doi.org/10.3390/met11081314

Lin, Y. C., Zhang, J., & Zhong, J. (2008). Application of neural networks to predict the elevated temperature flow behavior of a low alloy steel. *Computational Materials Science*, *43*(4), 752–758. Retrieved from https://doi.org/10.1016/j.commatsci.2008.01.039

Lourenço, R., Andrade-Campos, A., & Georgieva, P. (2022). The use of machine-learning techniques in material constitutive modelling for metal forming processes. *Metals*, *12*(3), 427. Retrieved from https://doi.org/10.3390/met12030427

Lu, J. Z., Zhong, J. W., Luo, K. Y., Zhang, L., Dai, F. Z., Chen, K. M., … Zhang, Y. K. (2011). Micro-structural strengthening mechanism of multiple laser shock processing impacts on AISI 8620 steel. *Materials Science and Engineering A*, *528*(19–20), 6128–6133. Retrieved from https://doi.org/10.1016/j.msea.2011.04.018

Ludwigson, D. C. (1971). Modified stress-strain relation for FCC metals and alloys. *Metallurgical Transactions*, *2*(10), 2825–2828. Retrieved from https://doi.org/10.1007/BF02813258

Ludwik, P. (1909). Elemente der Technologischen Mechanik. *Elemente der Technologischen Mechanik*. Berlin, German: Springer. Retrieved from https://doi.org/10.1007/978-3-662-40293-1

Mecking, H., & Kocks, U. F. (1981). Kinetics of flow and strain-hardening. *Acta Metallurgica*, *29*(11), 1865–1875. Retrieved from https://doi.org/10.1016/0001-6160(81)90112-7

Mirzadeh, H., Alibeyki, M., & Najafi, M. (2017). Unraveling the initial microstructure effects on mechanical properties and work-hardening capacity of dual-phase steel. *Metallurgical and Materials Transactions A: Physical Metallurgy and Materials Science*, *48*(10), 4565–4573. Retrieved from https://doi.org/10.1007/s11661-017-4246-z

Mondal, C., Singh, A. K., Mukhopadhyay, A. K., & Chattopadhyay, K. (2013). Tensile flow and work hardening behavior of hot cross-rolled AA7010 aluminum alloy sheets. *Materials Science and Engineering A*, *577*, 87–100. Retrieved from https://doi.org/10.1016/j.msea.2013.03.079

Nasiri, Z., & Mirzadeh, H. (2018). Enhancement of work-hardening behavior of dual phase steel by heat treatment. *Materialwissenschaft Und Werkstoff technik*, *49*(9), 1081–1086. Retrieved from https://doi.org/10.1002/mawe.201700122

Pandre, S., Mhatre, V., Kotkunde, N., & Kumar Singh, S. (2019). Strain hardening behavior of DP 590 steel using dislocation density based Kock-Mecking model. *Materials Today: Proceedings*, *46*, 9323–9327. Retrieved from https://doi.org/10.1016/j.matpr.2020.02.810

Poole, W. J., Embury, J. D., & Lloyd, D. J. (2011). Work hardening in aluminium alloys. *Fundamentals of Aluminium Metallurgy* (pp. 307–344). Berlin, Germany: Elsevier.

Rollett, A. D., & Kocks, U. F. (1993). A review of the stages of work hardening. *Solid State Phenomena*, *35–36*, 1–18. Retrieved from https://doi.org/10.4028/www.scientific.net/ssp.35-36.1

Sabokpa, O., Zarei-Hanzaki, A., Abedi, H. R., & Haghdadi, N. (2012). Artificial neural network modeling to predict the high temperature flow behavior of an AZ81 magnesium alloy. *Materials and Design*, *39*, 390–396. Retrieved from https://doi.org/10.1016/j.matdes.2012.03.002

Son, Y. Il, Lee, Y. K., Park, K. T., Lee, C. S., & Shin, D. H. (2005). Ultrafine grained ferrite-martensite dual phase steels fabricated via equal channel angular pressing: Microstructure and tensile properties. *Acta Materialia*, *53*(11), 3125–3134. Retrieved from https://doi.org/10.1016/j.actamat.2005.02.015

Swift, H. W. (1952). Plastic instability under plane stress. *Journal of the Mechanics and Physics of Solids*, *1*(1), 1–18. Retrieved from https://doi.org/10.1016/ 0022-5096(52)90002-1

Tabur, M., Izciler, M., Gul, F., & Karacan, I. (2009). Abrasive wear behavior of boronized AISI 8620 steel. *Wear*, *266*(11–12), 1106–1112. Retrieved from https://doi.org/10.1016/j.wear.2009.03.006

Tomita, Y., & Okabayashi, K. (1985). Tensile stress-strain analysis of cold worked metals and steels and dual-phase steels. *Metallurgical Transactions A*, *16*(5), 865–872. Retrieved from https://doi.org/10.1007/BF02814837

Voce. (1948). The relationship between stress and strain from homogenous deformation. *Journal of the Institute for Metals*, *74*, 537–562.